Design of Miniaturized Wireless Power Receivers for mm-sized Implants

Chul Kim[1], Sohmyung Ha[2], Abraham Akinin[1], Jiwoong Park[1], Rajkumar Kubendran[1], Hui Wang[1], Patrick P. Mercier[1], and Gert Cauwenberghs[1]
[1]University of California San Diego, La Jolla, CA 92093
[2]New York University Abu Dhabi, Abu Dhabi, UAE 129188

***Abstract*—Advances in free-floating miniature medical implants promise to offer greater effectiveness, safety, endurance, and robustness than today's prevailing medical implants. Wireless power transfer (WPT) is key to miniaturized implants by eliminating the need for bulky batteries. This paper reviews design strategies for WPT with mm-sized implants focusing on resonant electromagnetic and ultrasonic transmission. While ultrasonic WPT offers shorter wavelengths for sub-mm implants, electromagnetic WPT above 100 MHz offers superior power transfer and conversion efficiency owing to better impedance matching through inhomogeneous tissue. Electromagnetic WPT also allows for fully integrating the entire wireless power receiver system with an on-chip coil. Attaining high power transfer efficiency requires careful design of the integrated coil geometry for high quality factor as well as loop-free power and signal distribution routing to avoid eddy currents. Regulating rectifiers have improved power and voltage conversion efficiency by combining the two RF to DC conversion steps into a single process. Example designs of regulating rectifiers for fully integrated wireless power receivers are presented.**

I. Introduction

Miniaturization of implants to millimeter dimensions as illustrated in Fig. 1 opens up new possibilities to long-lasting, robust, and information-rich brain-machine interface (BMI) technologies. BMI technologies with current implantable devices offering limited operation time (months to a year) have proven their potential. For instance, recent BMI research successfully demonstrates recovery from spinal cord injuries [1]. Thus, there is a great interest in the medical community for the development of long-term and unobtrusive BMIs to enable quality of life improvements for patients suffering from debilitating conditions. Miniature implants overcome a major obstacle to the longevity of BMI technologies, as reduced micro-motions result in less astroglial scarring, and cell death [2]–[5]. In addition, miniature implants can be modularly deployed to extend their coverage to the entire cortical surface while maintaining high spatial resolution [6], [7].

The biggest component by volume in conventional implants is typically the battery. Ideally, the total size of an implant for BMI should be mainly limited by the physical requirements of the sensor and functional electronics rather than that of the energy source. Therefore, bulky batteries are not an acceptable solution to power implants for BMI. Wireless power transfer (WPT) offers a viable alternative to battery power, by enabling drastic miniaturization and extended life time of the implant [8].

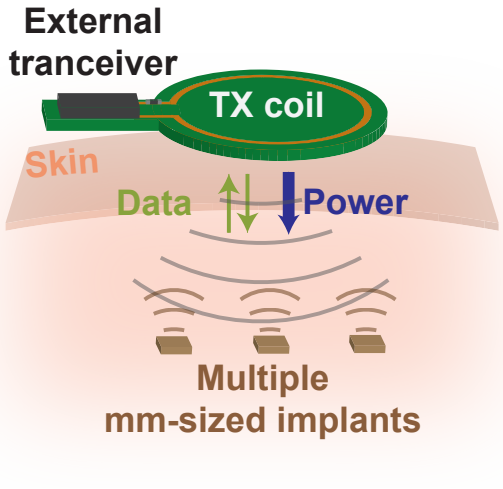

Fig. 1. Wireless power transfer and bi-directional data communication with multiple mm-sized implants served by a single external transceiver.

However, miniaturization to mm dimensions is still challenging because a plurality of up-to-date current WPT techniques still rely on bulky external power receiving (RX) coils and energy-storage decoupling capacitors. Thus, implementation of WPT with a small form factor for mm-sized implants persists as an unresolved issue. Ultimate miniaturization can be truly enabled by integrating those external bulky components into an free-floating on-chip wireless power receiver.

This paper reviews two major WPT modalities for mm-sized implants in Sec. II, and discusses main design considerations for fully integrated wireless power receivers in Sec. III. In Sec. IV, two state-of-the-art regulating rectifiers applicable to miniaturized wireless power receiver with an on-chip coil are presented with measurement results, followed by a performance comparison and conclusions in Sec. V.

II. Wireless Power Transfer Modalities for Miniaturized Implants

Two different WPT modalities have been widely investigated for mm-sized implants: WPT using either electromagnetic or ultrasound waves. Baseline mechanisms, advantages and disadvantages are discussed for each of these two modalities in the following section.

978-1-5090-5191-5/17/$31.00@2017 IEEE

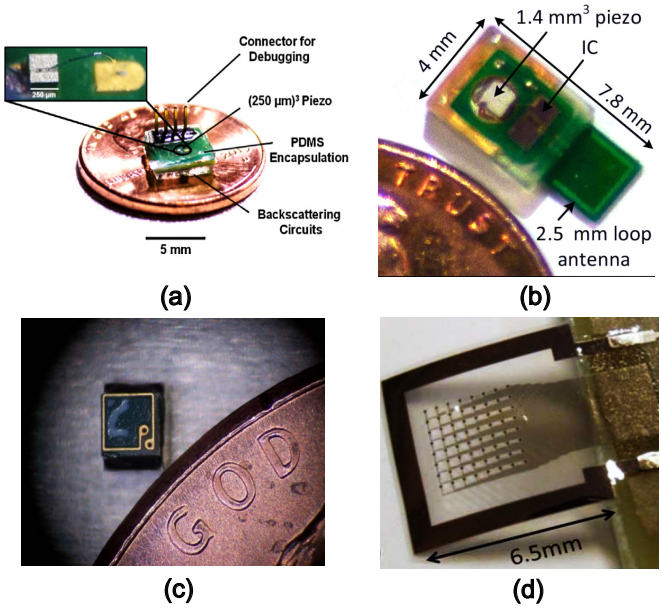

Fig. 2. Example mm-sized implants with ultrasonic and electromagnetic WPT modalities. Ultrasonic WPTs with: (a) 250 μm^3 piezo transducer and backscattering circuits composing of several discrete components [11]; and (b) a 1.4 mm^3 piezo transducer, a 1 mm $\times$ 2 mm chip, and a 2.5 mm $\times$ 2.5 mm off-chip RF antenna for data communication [12]. Electromagnetic WPTs with: (c) 1 mm $\times$ 1 mm 535 MHz RX coil connected to the same size CMOS IC beneath [13]; and (d) 6.5 mm $\times$ 6.5 mm 300 MHz RX coil and 64 channel electrode array [7].

A. Ultrasonic Wireless Power Transfer

For ultrasonic WPT, power transmitting (TX) and receiving (RX) parts are implemented with piezoelectric transducers for conversion between electrical and acoustic energy. On the TX side, electrical energy is converted to a pressure wave, which is then transcutaneously transmitted to the RX side (implants) through the media. The RX transducer converts part of the received acoustic energy back to electrical form [9]. Owing to relatively slow speed of propagation ($\approx$ 1540 m/s in human soft-tissue), ultrasound offers a wavelength comparable ($\approx$ 1.5 mm at 1 MHz of operating frequency) to the mm-sized implant dimensions. The matched wavelength and implant dimensions allow for focal power delivery resulting in efficient coupling efficiency [10]. Correspondingly, recent studies successfully demonstrated ultrasonic WPT delivery of up to 100 μW to mm-sized implants at cm-range separation between TX and RX as shown in Fig. 2 (a) [11] and (b) [12].

Despite great advantages, applications of ultrasonic WPT to implants are limited. As the ultrasonic pressure wave travels toward the implant, it traverses several layers of tissue with substantial differences in acoustic impedances. Crossing tissue boundaries causes reflections of the pressure wave proportional in amplitude to the degree of acoustic impedance mismatch. While such reflections are highly beneficial as the key principle in ultrasonographic imaging, they deteriorate the energy coupling efficiency in WTP applications. For example, the acoustic impedance of skull is more than 4.6 times greater than that of adjacent soft tissue layers, causing a pressure reflection ratio of 0.64, and resulting in less than 2% of the incident power making it across towards a transcranial implant [14], [15]. As such, ultrasonic WPT is only effective for powering implants where there is little to negligible acoustic impedance mismatch in the path from TX to the implant. The reach of ultrasonic WPT could however be extended, in principle, by inserting repeaters at impedance mismatch boundaries. For instance, to avoid the huge power losses due to skull reflection, a WPT hub sub-cranial interrogator can be inserted under the skull combining electromagnetic WPT to an external transceiver above, with ultrasonic WPT to mm-sized implants underneath [11]. Typical currently achievable transfer efficiencies from WPT interrogators to mm-sized implants at cm-range distances are less than 0.1 % due in part to severe size limits in both piezo transducers. In addition to power delivery, data communication via ultrasound has a limited data rate due to its relatively low operating frequency ($\leq$ 10 MHz). To improve up-link (from implants to external transceiver) data rates to several Mbps, 4 GHz ultra-wideband (UWB) RF communication has been employed with an additional PCB loop antenna [12].

It is worth mentioning also that most of current state-of-the-art ultrasonic WPTs employ lead zirconate titanate (PZT) which offers high transfer efficiency owing to its superior electromechanical coupling coefficient compared to other piezo-materials. Unfortunately, PZT components included in implants pose significant health risks of long-term lead exposure inside the human body. These and other current challenges of ultrasonic WPT will likely be overcome with future research advances in materials and integrated circuit design.

B. Electromagnetic Wireless Power Transfer

Electromagnetic (EM) WPT is currently most commonly adopted with mm-sized implants. EM WPT requires TX and RX coils to be inductively coupled through matching resonant tanks for wireless power delivery. Due to the miniature size of the implant, the tank resonance condition requires the addition of lumped capacitance to the coil inductance, requiring careful sizing considerations. The TX coil produces a time varying magnetic flux, which is shared with the RX coil where an electromotive force (EMF) is generated. Since the EMF is directly proportional to the area of RX coil by Faraday's law of induction, the size of the RX coil often dominates the size of implants for better WPT performance. The challenge with miniaturized implants is then to minimize the size of the RX coil without greatly compromising WPT performance. A common strategy is to increase the operating frequency of the implant resonant tank, which increases induction via higher time-varying rate of magnetic flux, and increases quality (Q) factors of both TX and RX coils. A higher operating frequency, however, also increases tissue absorption of the incident electromagnetic radiation, and thus reduces the maximum transmittable power to the implant under the regulations of Specific Absorption Rate (SAR). As such, by balancing both effects, operating frequencies from 100 MHz to 1 GHz have

proven optimal for EM WPT to mm-sized implants. [7], [13], [16]–[19]. Examples of mm-sized implants utilizing EM WPT operating in this range of resonant frequencies are shown in Fig. 2 (c) and (d).

Operating frequencies above 100 MHz open up the possibility of full integration of the RX coil directly on chip with a standard CMOS process. This integration offers significant advantages to mm-sized implants: *i)* ultimate miniaturization of implants by eliminating the space previously occupied by the RX coil, *ii)* no special fabrication process is needed to implement a RX coil, *iii)* greatly simplified encapsulation via removing any lines and connectors between the RX coil to the electronics, and *iv)* reduced parasitic capacitance and resistance between the RX coil and its fully integrated matching network (thereby eliminate additional power loss) [20]–[23]. Therefore, integration of RX coil on-chip is a significant step toward free-floating miniaturized implants.

III. Design Considerations for Fully Integrated Inductive Wireless Power Receivers

While implementing an on-chip coil offers various advantages, it requires careful design of the wireless power receiver to optimize the WPT system efficiency (WSE), defined as the ratio of RX power delivered to the load to the TX transmitted power. WSE is an overall measure accounting for several factors in the WPT system, including two important factors on the implant side: the efficiency of the TX-RX inductive link, and the efficiency of RX RF-to-DC conversion. These two factors are described in turn in the following sections, with a figure-of-merit account of overall WSE for comparison with the state-of-the-art in Sec. IV-C.

A. RX Coil Design

The maximum achievable TX-RX link efficiency, and hence WSE, depends strongly on the coupling coefficient k. To first order, the coupling coefficient k depends on coil geometry and separation distance between TX and RX coil, which are mostly given by the application [24]. Controllable design parameters in maximizing WSE are mainly the Q factors of TX and RX coils, both of which should be maximized. Optimal design of the on-chip RX coil is of paramount importance since the Q of the RX coil is limited more stringently compared to that of TX coil [16].

As a guiding principle, the on-chip RX coil is implemented with thick top-layer metal at the chip boundaries to maximize its area (for better coupling coefficient, k) and to minimize its parasitic resistance (for higher Q factor) and parasitic capacitance to substrate (for minimum losses and higher self-resonance frequency).

The number of turns of the RX coil critically affects its Q factor. At a given resonant frequency, a higher number of turns leads to a larger coil inductance and smaller matching capacitance of the LC tank. To first order, the inductance of the coil is proportional to the square of the number of turns while parasitic series resistance increases with the number of turns. As such, Q tends to increase with number of turns at certain frequency range. If large number of metal stacks are supported in the process, then series connections of two or three top-layer metal lines can be used to increase the effective number of turns within the space constraints [21]. Likewise, multiple metal layers in parallel can reduce sheet resistance of the RX coil to improve Q factor.

At large number of turns or at higher frequencies, however, Q tends to decrease rather than increase with the number of turns because the increased parasitic capacitance results in a lower self-resonance frequency. Furthermore, a many-turn coil offers larger voltage swing but limited current driving capability at the LC tank. This induces circuit design difficulties where the load implied by the implant circuits draws sparse but instantly large current out of the LC tank, such as for electrical stimulation. Supply voltage generation at the rectifier and regulator may then fail due to significant voltage drop at the LC tank. Resonance with a smaller matching capacitor is also more vulnerable to any parasitic capacitance and fabrication mismatch.

In summary, designs with larger numbers of turns for the RX coil offer greater Q for greater WSE, but at the expense of vulnerabilities to parasitics. In practice, for typical mm-sized implants operating between 100 MHz and 300 MHz, between 2 and 4 turns are appropriate.

B. Power and Signal Distribution

One additional challenge in fully integrated WPT receivers arises due to the proximity of active electronics to the receiving coil. Eddy currents induced by the alternating magnetic field affect significant energy losses limiting the Q of the RF coil, and further affect the functioning of sensitive analog circuits in the implant. Eddy currents in the silicon substrate can be minimized by adopting a silicon-on-insulator (SOI) process; however eddy currents in metal layers potentially pose a more significant problem, requiring to pay extreme attention on metal routing near the coil.

In particular it is critically important to avoid any metal loops in the design and layout of all circuits in the implant chip. The main culprits in generating Q-reducing loops and large metal planes are often power and signal lines distributed across the entire chip such as ESD power supply lines connected to all pads or chip guard-ring metal, and congregated decoupling capacitors (decaps). These loops and metal planes induce eddy currents reducing Q factor of the RX coil by over 60% (thereby reducing WPT efficiency), while also introducing noise to sensitive circuits and a signal distribution network. To avoid large metal planes on-chip, [20] reduced decaps to only 20 pF through inclusion of a high-performance but high-power linear regulator on the wireless power receiver. A fractal H-tree power and signal distribution network with distributed decaps shown in Fig. 3 (a) is a practical solution to systematically remove all loops and large planes from the wireless power receiver [23]. This H-tree topology furthermore serves as a network backbone for eliminating differential mode interference in sensitive analog differential signals by ensuring equidistant signal paths. HFSS simulation and measurement

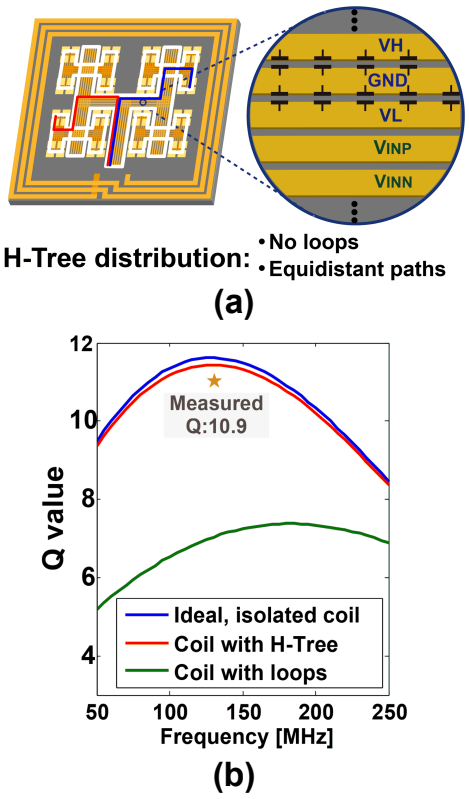

Fig. 3. Power and signal distribution for minimal RF interference in fully integrated mm-sized WPT. (a) Fractal low-loss H-Tree power and signal distribution network with energy-storage decoupling capacitors without loops and with equidistant signal paths (red and blue lines), and (b) simulated and measured Q factor of the RX coil [23].

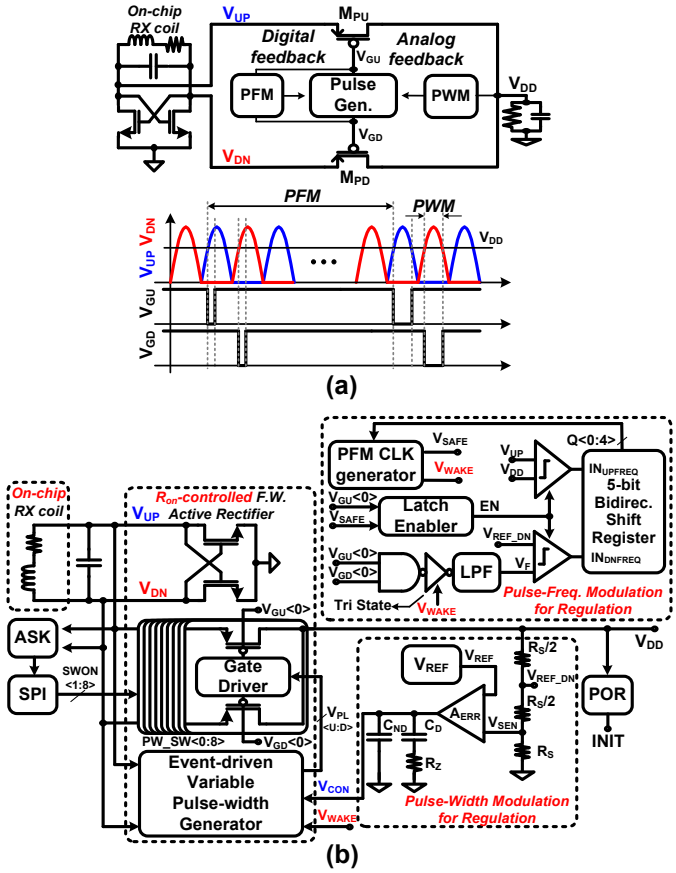

Fig. 4. Hybrid pulse modulation (HPM) with combined pulse-width modulation (PWM) and pulse-frequency modulation (PFM) for integrated resonant rectification and regulation (IR^3). (a) Conceptual operation and timing diagram. (b) Block-level IR^3 circuit diagram [22].

in Fig. 3 (b) show negligible loss in Q compared to an ideal, isolated coil, such that most of the incident RF energy directly couples to the RX coil rather than the metal traces cohabiting the chip. Hence, with H-tree power and signal distribution on a wireless power receiver, WSE is maximized while also decoupling RF interference.

IV. RF-DC Conversion: Regulating Rectifiers

An integrated regulating rectifier accomplishes simultaneous rectification of the RF input and regulation of the DC, in a single step. As such, it improves power conversion efficiency (PCE) and voltage conversion efficiency (VCE) by eliminating losses in a separate regulation step. For regulation, a standalone low-drop-out (LDO) is commonly employed, which often is the most power consuming block [12] and [13]. The following section presents two example designs of regulating rectifiers operating with on-chip RX coil for mm-sized implants, along with a comparison with the state-of-the-art.

A. Integrated Resonant Regulating Rectifier

A CMOS fully-integrated resonant regulating rectifier (IR^3) for inductive power telemetry in mm-sized implantable devices was presented in [22]. To counter disadvantages of cascaded two-stage conversion, a fully integrated solution to combined rectification and regulation directly coupling the on-chip resonant tank to the on-chip load, by hybrid pulse-width modulation (PWM) and pulse-frequency modulation (PFM) of the conductive path between the tank and the load as illustrated in Fig. 4 (a) was proposed for IR^3. Each pulse activates a conductive path between the resonant tank and the load, accomplishing both rectification and regulation in one step. For rectification, the pulse generator in Fig. 4 (a) activates the up-rectifying power PMOS transistor M_{PU} by lowering V_{GU} when its RF input, V_{UP}, exceeds V_{DD}. Conversely, the down-rectifying power PMOS transistor M_{PD} is activated by lowering V_{GD} when its RF input, V_{DN}, exceeds V_{DD} in the opposite RF phase for full-wave rectification. For regulation, the width of the activation pulse is controlled by PWM through analog feedback, and its pulse frequency is controlled by PFM through digital feedback.

The PWM module regulates V_{DD} simultaneously with rectification, by adjusting the pulse-width based on error accumulation between V_{SEN} (divided from V_{DD}) and a predefined reference voltage, V_{REF} shown in Fig. 4 (b). The PWM offers accurate regulation of V_{DD} since large loop gain analog feedback rejects static error in inputs of an error integrator,

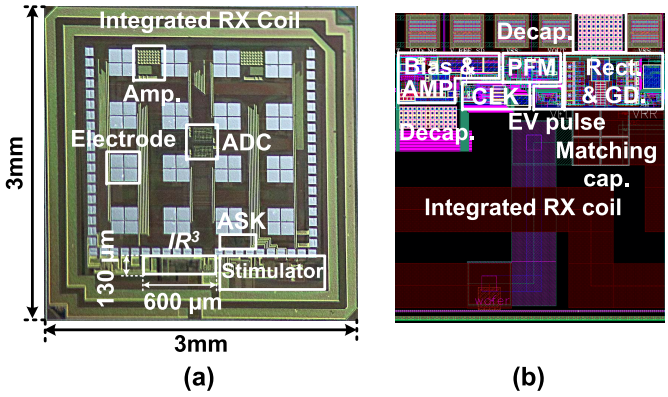

Fig. 5. (a) Microphotograph of a fully-integrated resonant regulating rectifier (IR^3) for inductive wireless power telemetry in mm-sized implantable devices, and (b) detailed layout of IR^3 [22].

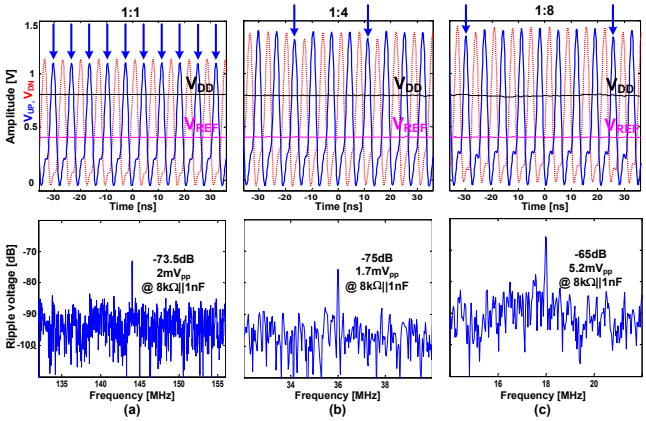

Fig. 6. Measured RF inputs and DC-regulated output under under 8 kΩ in parallel with 1 nF load operating in (a) 1:1 (144 MHz) mode, (b) 1:4 (144 MHz/4) mode, and (c) 1:8 (144 MHz/8) mode by HPM. Arrows indicate active cycles providing between the LC tank and the load. Spectra for voltage ripple in the regulated output V_{DD}, peaking at the operating frequency, are shown below for each [22].

A_{ERR}, by error integration. However, due to compensation with C_D,R_Z, and C_{ND} for stability of the analog feedback loop, response time of PWM analog feedback is relatively slow, in the range of several hundred microseconds. In addition, narrow pulse widths prohibit the IR^3 from achieving high PCE at light load conditions. As such, PWM alone is insufficient for accurate and efficient regulation.

To address these challenges and provide rapid digital feedback, another PFM regulation loop is included in addition to and in tandem with PWM. The PFM module increases the pulse frequency of V_{GU} and V_{GD} when either pulse width being regulated by PWM reaches an upper threshold; conversely, the pulse frequency is decreased when either pulse width reaches a lower threshold. As such, PFM together with PWM provides broad-range and rapid regulation and improved power conversion efficiency at light load conditions.

Fig. 4 (b) shows the block-level circuit diagram of the IR^3. The analog output V_{CON} of the PWM module and the digital output V_{WAKE} of the PFM modules control the width and frequency of the pulsed waveforms $V_{PL<U>}$ and $V_{PL<D>}$ driving the gates of up to nine parallel-connected power PMOS transistors. A power-on-reset generates an INIT signal forcing the IR^3 into passive mode with diode-connected PMOS transistors and initializing digital state variables in the PFM module during start-up [8].

A microphotograph of the mm-sized implantable system powered by the IR^3 and detailed layout of the IR^3 are shown in Fig. 5 (a) and (b), respectively. The active area of the IR^3 design is 0.078 mm^2 in 180 nm 1P4M SOI CMOS. An on-chip RX coil is implemented at the chip edge so as to maximize its area with two turn top metal for 23.7 nH inductance. Metal width of the coil is 100 μM for a small series resistance, R_{coil}, rendering around 12 of Q_{coil} with *HFSS* electromagnetic simulation. The IR^3 is located right after matching capacitor to reduce any possible parasitics.

Fig. 6 shows measurements of the IR^3 regulating V_{DD} at 0.8 V within 5.2 mVpp ripple for various frequency modulations under varying RF inputs from link variations such as distance differences between coils. As expected, the rate of rectification (i.e., PFM frequency) is maximum (i.e., 144 MHz) for small amount of RF input power, as the rectifier attempts to extract as much energy from the RF as possible in order to regulate the output (Fig. 6, (a)). On the other hand, the rate of rectification is much lower at high RF input power levels (Fig. 6, (c)), as a significant amount of energy can be extracted from the RX coil and the matching capacitor over a short period of time. These measurements demonstrate the effectiveness of the proposed hybrid pulse modulation technique.

B. Adaptive Buck-Boost Resonant Regulating Rectifier

The IR^3 has demonstrated complete on-chip integration of a regulating rectifier. For further improvement in robustness to wide RF input voltage range coming from link variations, a buck-boost resonant regulating rectifier (B^2R^3) was presented in [23]. The presented B^2R^3 accomplishes regulated rectification over wide input range through a mode arbiter that adapts to the sensed RF envelope, as illustrated in Fig. 7 (a). BOOST mode converts low RF voltage to larger regulated DC voltage, while BUCK1,2,3 modes efficiently convert larger RF voltage down. For smooth transition between modes, a combined BUCK-BOOST mode operates at an intermediate region. The B^2R^3 produces dual supply voltage, VH and VL, and is composed of boost and buck regulating rectifiers, a feedback part, and a distributed decoupling capacitors for each power supply and a shared block of mode arbiter for both supply voltages.

Circuit diagrams of the feedback unit, and the boost and buck regulating rectifiers, are shown Fig. 8. VHS tracks VH with DC offset generated by current source, I_S, and resistance R_S of two stacked diode-connected NMOS devices for defining a target VH as shown in Fig. 8 (a). To retain the fast settling of conventional integrator-less bang-bang control, VHS is directly fed to the latch (path 2) while a parallel integration path (path 1) with an OTA and compensation

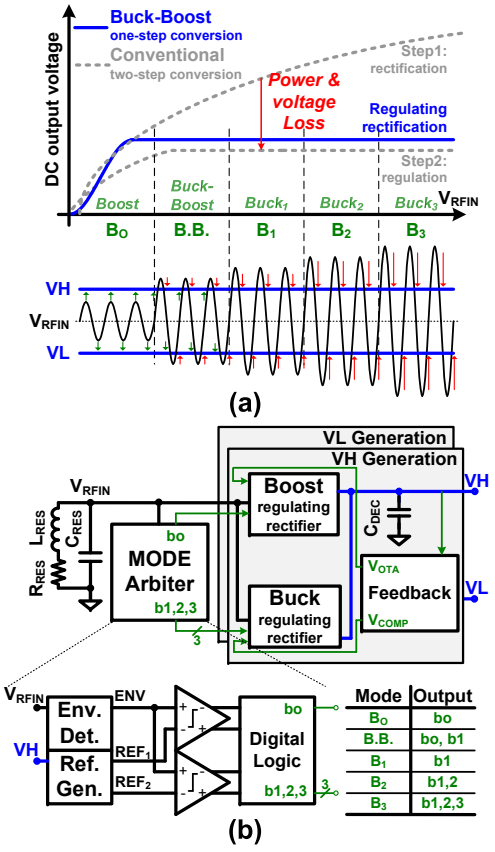

Fig. 7. (a) Conceptual operation of the conventional 2-step power conversion and the B^2R^3 showing the 5 regulating rectification modes that efficiently generate a dual supply according to RF input. (b) Overview block diagram of the adaptive B^2R^3 with mode arbiter [23].

components performs PID control to additionally remove static error at VH. The boost regulating rectifier employs a feedback-controlled $V_{\rm TH}$ cancellation scheme for regulation. The feedback loop dynamically determines the amount of $V_{\rm TH}$ cancellation through $V_{\rm OTA}$. The switched capacitor circuits shown in Fig. 8 (b) implement floating voltage sources by transferring $V_{\rm OTA}$ to the NMOS devices in the boost rectifier, such that bias point of the NMOS devices is dynamically decided regarding on RF input power and load condition. A zero short-circuit-current level-shifter performs suppy domain conversion from VH to internally generated higher voltage, VHH while consuming 190 nW at 1 MHz. The buck regulating rectifier is activated by output of the latch $V_{\rm COMP}$ in the feedback unit. The regulating rectifier dynamically determines the duty-cycle of the active switches (i.e., t_d and $t_{\rm pw}$) with a local feedback composing of delay controlled inverter chains and latches operating at 1 MHz for maximizing $t_{\rm pw}$. To prevent undesired energy transfer from large RF input, the power PMOSs are gated with a voltage (VHH) larger than the RF envelope. Three power switches are implemented in parallel (BUCK1,2,3) to optimize PCE according to RF input.

A microphotograph of the 3 mm $\times$ 3 mm sized implantable wireless power receiver and detailed layout of the power-

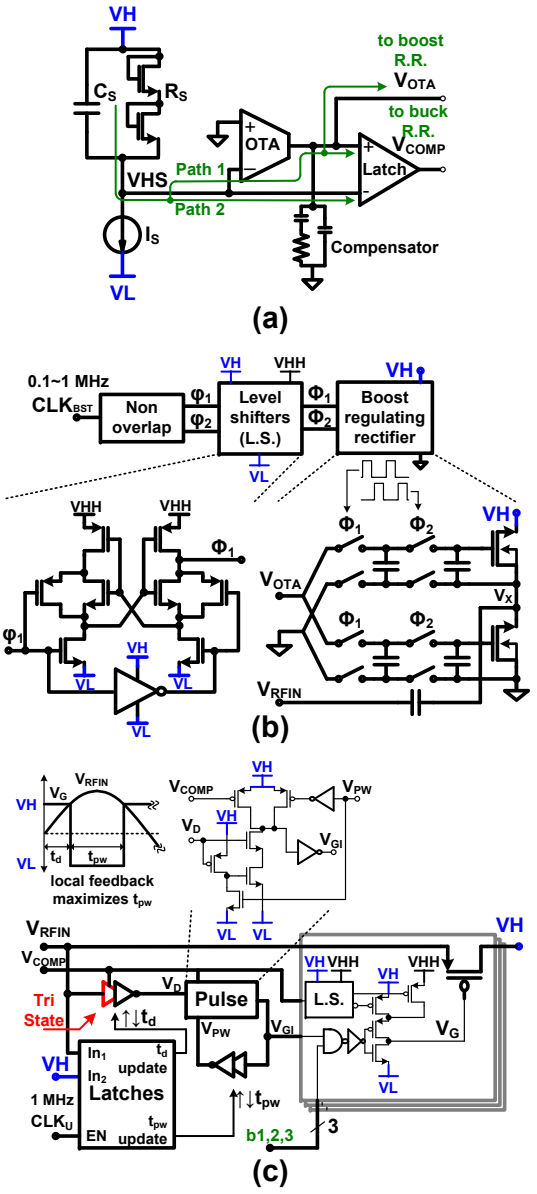

Fig. 8. (a) Conceptual operation of the conventional 2-step power conversion and the B^2R^3 showing the 5 regulating rectification modes that efficiently generate a dual supply according to RF input. (b) Overview block diagram of the adaptive B^2R^3 with mode arbiter [23].

management blocks, B^2R^3, are shown in Fig. 9 (a) and (b), respectively. A three-turn on-chip RX coil is integrated with the top metal routing in 180 CMOS SOI process offering 60.3 nH of inductance with 10.9 of Q factor. Active area of B^2R^3 is 0.194 mm^2, which is slightly larger than that of the IR^3 in Sec. IV-A due largely to the area of mode arbiter and boost regulating rectifier. Owing to these extra blocks for mode adaptation, the B^2R^3 produces regulated output voltages even under highly dynamic input conditions such as 50 % amplitude variation in PA input, as shown in Fig. 10 (a) and (b). This mode adaptation is important since the RF input power can vary substantially for a number of reasons such as variations

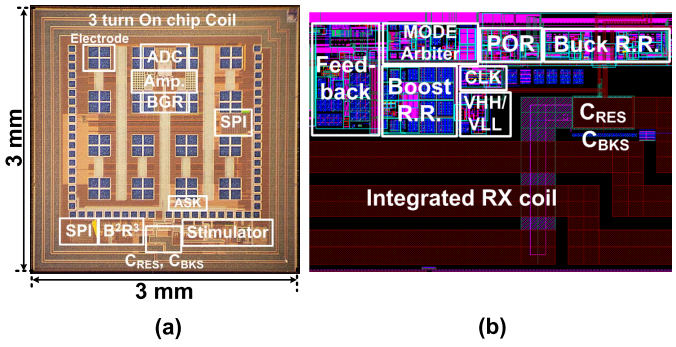

Fig. 9. (a) Microphotograph of a 3 mm × 3 mm implantable WPT system with adaptive buck-boost resonant regulating rectifier (B^2R^3) and low-loss H-Tree power and signal distribution, and (b) detailed layout of B^2R^3. Active silicon area for B^2R^3 is 0.194 mm^2 [23].

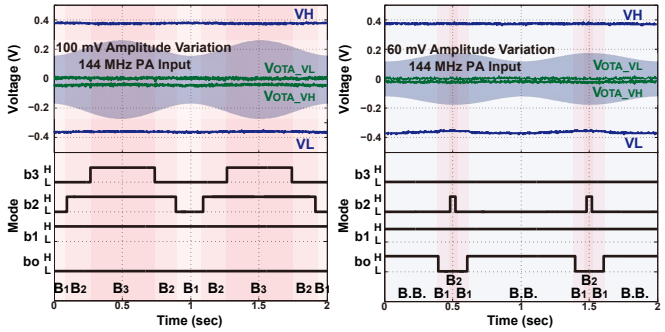

Fig. 10. Dynamic RF input regulation capability is characterized under (a) 100 mV and (b) 60 mV amplitude variations at power amplifier (PA) input [23].

in link distance, alignment, and impedance.

C. Comparison with state-of-the-art designs

Table I summarizes key performance measures in comparison with the state of the art. The table shows IR^3 and B^2R^3 are the only fully integrated mm-sized WPT receivers with regulating rectifier for one-step power conversion at higher than 100 MHz resonant frequency. It is important to note that link efficiency from TX coil to RX coil is inversely proportional to the cube of the distance between TX and RX coils [18] and the cube of the square root of the area of RX coil [21] for the case of mm-sized RX coil. For a fair comparison to the state-of-the-art designs, normalizing for TX-RX distances (typically ranging 5-15 mm), and for RX diameters (typically ranging 1-8 mm), a figure-of-merit (FoM) was proposed by [21]. However, this FoM takes only link efficiency from TX to RX coil into account. Hence, an adjusted FoM that accounts for full WPT system efficiency (WSE) from TX coil to regulated DC rather than WPT link efficiency was proposed in [23]:

$$\text{WPT system efficiency FoM} = \frac{\text{WPT system efficiency} \times D^3}{A^{1.5}} \quad (1)$$

where D is the distance between two TX and RX coils, and A is the area of the RX coil (outer dimension) [23]. The two presented regulating rectifiers in Secs. IV-A and IV-B offer WSE FoM of 80.3 and 102.1, respectively.

V. Conclusion

Miniaturization of implants enables long-term and robust BMI technologies by improving their longevity, safety, and high spatial resolution. This review highlighted two major WPT methods for mm-sized implants: ultrasonic WPT and electromagnetic WPT. While ultrasonic WPT offers advantages particularly for sub-mm implants, electromagnetic WPT is superior for BMI applications, as it is better suited for transcranial transmission and can support higher data rates. Critical design considerations for optimal integration of RX coils on-chip include sizing and number of turns of the coil, and H-tree power and signal distribution. Two example designs for regulating rectifiers operating as fully integrated wireless power receivers were presented with high WPT system efficiency figure-of-merit. As a significant advancement in miniaturization, fully integrated wireless power receivers enable next-generation modular mm-sized wireless implants. On-going and future research directions include closed-loop communication between external beamforming transceiver and distributed modular implants [25], [26].

References

[1] M. Capogrosso, T. Milekovic, D. Borton, F. Wagner, E. M. Moraud, J.-B. Mignardot, N. Buse, J. Gandar, Q. Barraud, D. Xing, E. Rey, S. Duis, Y. Jianzhong, W. K. D. Ko, Q. Li, P. Detemple, T. Denison, S. Micera, E. Bezard, J. Bloch, and G. Courtine, "A brainspine interface alleviating gait deficits after spinal cord injury in primates," *Nature*, vol. 539, pp. 284–288, 11 2016.

[2] S. S. Polikov, P. A. Tresco, and W. M. Reichert, "Response of brain tissue to chronically implanted neural electrodes," *Journal of Neuroscience Methods*, vol. 148, no. 1, pp. 1–18, 2005.

[3] H. Lee, R. V. Bellamkonda, W. Sun, and M. E. Levenston, "Biomechanical analysis of silicon microelectrode-induced strain in the brain," *Journal of Neural Engineering*, vol. 2, pp. 81–89, Dec. 2005.

[4] G. C. McConnell, H. D. Rees, A. I. Levey, C.-A. Gutekunst, R. E. Gross, and R. V. Bellamkonda, "Implanted neural electrodes cause chronic, local inflammation that is correlated with local neurodegeneration," *Journal of Neural Engineering*, vol. 6, October 2009.

[5] L. Karumbaiah, T. Saxena, D. Carlson, K. Patil, R. Patkar, E. A. Gaupp, M. Betancur, G. B. Stanley, L. Carin, and R. V. Bellamkonda, "Relationship between intracortical electrode design and chronic recording function," *Biomaterials*, vol. 34, pp. 8061–8074, November 2013.

[6] S. Ha, A. Akinin, J. Park, C. Kim, H. Wang, C. Maier, P. P. Mercier, and G. Cauwenberghs, "Silicon-integrated high-density electrocortical interfaces," *Proceedings of the IEEE*, no. 99, pp. 1–23, 2016.

[7] R. Muller, H.-P. Le, W. Li, P. Ledochowitsch, S. Gambini, T. Bjorninen, A. Koralek, J. Carmena, M. Maharbiz, E. Alon, and J. Rabaey, "A Minimally Invasive 64-Channel Wireless μECoG Implant," *IEEE Journal of Solid-State Circuits*, vol. 50, pp. 344–359, Jan. 2015.

[8] H.-M. Lee and M. Ghovanloo, "A high frequency active voltage doubler in standard cmos using offset-controlled comparators for inductive power transmission," *IEEE Transactions on Biomedical Circuits and Systems*, vol. 7, pp. 213–224, June 2013.

[9] S. Ozeri and D. Shmilovitz, "Ultrasonic transcutaneous energy transfer for powering implanted devices," *Ultrasonics*, vol. 50, no. 6, pp. 556–566, 2010.

[10] M. D. Menz, . Oralkan, P. T. Khuri-Yakub, and S. A. Baccus, "Precise neural stimulation in the retina using focused ultrasound," *Journal of Neuroscience*, vol. 33, no. 10, pp. 4550–4560, 2013.

[11] D. Seo, J. M. Carmena, J. M. Rabaey, M. M. Maharbiz, and E. Alon, "Model validation of untethered, ultrasonic neural dust motes for cortical recording," *Journal of Neuroscience Methods*, vol. 244, pp. 114–122, 2015.

TABLE I
PERFORMANCE COMPARISON

	Seo [11]	Charthad [12]	Muller [7]	Zargham [20, 21]	Mark [13, 19]	O'Driscoll [17]	Kim [22]	Kim [23]
WPT method	ultrasonic	ultrasonic	EM	EM	EM	EM	EM	EM
Dimension (mm^2)	5.06	31.2	43.97	4.84[a]	1[a]	4.37[a]	9	9
Operating Freq. (MHz)	6.1	1	300	160	535	915	144	144
Power RX/ dimension /location (Value (nH))	PZT/ 0.015 mm^3 /off-chip	PZT/ 1.4 mm^3 /off-chip	Coil/ 42.25 mm^2 /off-chip (32)	Coil/ 4.36 mm^2 /on-chip (130)	Off-chip/ 1 mm^2 /off-chip (5.73)	Off-chip/ 4 mm^2 /off-chip (N.R.)	On-chip/ 8.64 mm^2 /on-chip (23.7)	On-chip/ 8.74 mm^2 /on-chip (60.3)
Regulator	Not needed	separate LDO	separate LDO	separate LDO	separate LDO	separate LDO	regulating rectifier	regulating rectifier
Dec. Cap (nF)	Not needed	3.3	4	0.02	1.39	N/R	1	0.25
Process	Discrete	65 nm CMOS	65 nm CMOS	0.13 µm CMOS	65 nm CMOS	0.13 µm CMOS	0.18 µm CMOS SOI	0.18 µm CMOS SOI
WSE* (%)	< 0.1[b]	N/R	1.19[b]	0.62[c]	0.02 (-37 dB)	0.048 (-33.2 dB)	2.04	2.64
Distance (mm)	30	30	12.5	10	13	15	10	10
WSE FoM**	Not applicable	Not applicable	8.46	68.1	43.94	20.25	80.3	102.1

[a]not include data communication

[b]TX PZT transducer to RX PZT transducer

[c]estimated from provided data, TX PW: 13mW, P_{DC_LOAD}: 0.160mW

[d]estimated from provided data, estimated η_{LDO}: 68 % (V_{DD}: 3.1 V, V_{REC2}: 4.5 V), η from TX to the rectifier: 0.9 %

*WSE = WPT system efficiency (from TX to regulated DC)

**WPT System Efficiency FoM = $\frac{\eta_{overall} \times D^3}{A^{1.5}}$,where $\eta_{overall}$ is TX-regulated DC efficiency;

D is distance between TX-RX coils; and A is area of the RX coil.

[12] J. Charthad, M. J. Weber, T. C. Chang, and A. Arbabian, "A mm-sized implantable medical device (imd) with ultrasonic power transfer and a hybrid bi-directional data link," *IEEE Journal of Solid-State Circuits*, vol. 50, pp. 1741–1753, Aug 2015.

[13] M. Mark, *Powering mm-Size Wireless Implants for Brain-Machine Interfaces*. PhD thesis, Electrical Engineering and Computer Sciences, University of California at Berkeley, December 2011.

[14] P. N. T. Wells, *Biomedical ultrasonics*. Academic Press, 1977.

[15] E. E. Christensen, T. S. Curry III, and J. E. Dowdey, *An Introduction to the Physics of Diagnostic Radiology, Second Edition*. Lea & Febiger, 1978.

[16] D. Ahn and M. Ghovanloo, "Optimal design of wireless power transmission links for millimeter-sized biomedical implants," *IEEE Transactions on Biomedical Circuits and Systems*, vol. 10, pp. 125–137, Feb. 2016.

[17] S. O'Driscoll, A. Poon, and T. Meng, "A mm-sized implantable power receiver with adaptive link compensation," in *IEEE International Solid-State Circuits Conference Digest of Technical Papers (ISSCC)*, pp. 294–295, 2009.

[18] A. Poon, S. O'Driscoll, and T. Meng, "Optimal frequency for wireless power transmission into dispersive tissue," *IEEE Transactions on Antennas and Propagation*, vol. 58, pp. 1739–1750, May 2010.

[19] M. Mark, Y. Chen, C. Sutardja, C. Tang, S. Gowda, M. Wagner, D. Werthimer, and J. Rabaey, "A $1mm^3$ 2 Mbps 330fJ/b Transponder for Implanted Neural Sensors," in *Symposium on VLSI Circuits (VLSI Circuits)*, pp. 168–169, 2011.

[20] M. Zargham and P. Gulak, "A 0.13 μm CMOS integrated wireless power receiver for biomedical applications," in *European Solid State Circuits Conference (ESSCIRC)*, pp. 137–140, 2013.

[21] M. Zargham and P. Gulak, "Fully integrated on-chip coil in 0.13 μm cmos for wireless power transfer through biological media," *IEEE Transactions on Biomedical Circuits and Systems*, vol. 9, pp. 259–271, April 2015.

[22] C. Kim, S. Ha, J. Park, A. Akinin, P. Mercier, and G. Cauwenberghs, "A 144 MHz integrated resonant regulating rectifier with hybrid pulse modulation," in *Symposium on VLSI Circuits (VLSI Circuits)*, pp. 284–285, 2015.

[23] C. Kim, J. Park, A. Akinin, S. Ha, P. P. Mercier, and G. Cauwenberghs, "A fully integrated 144 MHz wireless-power-receiver-on-chip with an adaptive buck-boost regulating rectifier and low-loss h-tree signal distribution," in *Symposium on VLSI Circuits (VLSI Circuits)*, pp. 284–285, 2016.

[24] R. Sarpeshkar, *Ultra Low Power Bioelectronics*. Cambridge: University Press, 2010.

[25] C. Kim, S. Joshi, C. Thomas, S. Ha, L. Larson, and G. Cauwenberghs, "A 1.3 mW 48 MHz 4-channel MIMO baseband receiver with 65 dB harmonic rejection and 48.5 dB spatial signal separation," *IEEE Journal of Solid State Circuits*, April 2016.

[26] D. Seo, H. Y. Tang, J. M. Carmena, J. M. Rabaey, E. Alon, B. E. Boser, and M. M. Maharbiz, "Ultrasonic beamforming system for interrogating multiple implantable sensors," in *2015 37th Annual International Conference of the IEEE Engineering in Medicine and Biology Society (EMBC)*, pp. 2673–2676, 2015.